



On the turbulent heat fluxes: A comparison among satellite-based estimates, atmospheric reanalyses, and *in-situ* observations during the winter climate over Arctic sea ice

Zhi-Lun ZHANG^{a,b,c}, Feng-Ming HUI^{a,b,c,*}, Timo VIHMA^d, Mats A. GRANSKOG^e,
Bin CHENG^d, Zhuo-Qi CHEN^{a,b,c}, Xiao CHENG^{a,b,c}

^a School of Geospatial Engineering and Science, Sun Yat-sen University, Southern Marine Science and Engineering Guangdong Laboratory (Zhuhai), Zhuhai 519082, China

^b Key Laboratory of Comprehensive Observation of Polar Environment (Sun Yat-sen University), Ministry of Education, Zhuhai 519082, China

^c University Corporation for Polar Research, Beijing 100032, China

^d Finnish Meteorological Institute, Helsinki 00560, Finland

^e Norwegian Polar Institute, Fram Centre, Tromsø N-9296, Norway

Received 21 September 2022; revised 3 April 2023; accepted 11 April 2023

Available online 17 April 2023

Abstract

The surface energy budget is crucial for Arctic sea ice mass balance calculation and climate systems, among which turbulent heat fluxes significantly affect the air–sea exchanges of heat and moisture in the atmospheric boundary layer. Satellite observations (e.g. CERES and APP-X) and atmospheric reanalyses (e.g., ERA5) are often used to represent components of the energy budget at regional and pan-Arctic scales. However, the uncertainties of the satellite-based turbulent heat fluxes are largely unknown, and cross-comparisons with reanalysis data and *in-situ* observations are limited. In this study, satellite-based turbulent heat fluxes were assessed against *in-situ* observations from the N-ICE2015 drifting ice station (north of Svalbard, January–June 2015) and ERA5 reanalysis. The turbulent heat fluxes were calculated by two approaches using the satellite-based ice surface temperature and radiative fluxes, surface atmospheric parameters from ERA5, and snow/sea ice thickness from the pan-Arctic Ice Ocean Modeling and Assimilation System (PIOMAS). We found that the bulk-aerodynamic formula based results could better capture the variations of turbulent heat fluxes, while the maximum entropy production based estimates are comparable with ERA5 in terms of root-mean-square error (RMSE). CERES-based estimates outperform the APP-X-based ones but ERA5 performs the best in all seasons (RMSE of 18 and 7 W m⁻² for sensible and latent heat flux, respectively). The air–ice temperature/humidity differences and the surface radiation budget were found the primary driving factors in the bulk-formula method and maximum entropy production (MEP) method, respectively. Furthermore, errors in the surface and near-surface temperature and humidity explain almost 50% of the uncertainties in the estimates based on the bulk-formula, whereas errors in the net radiative fluxes explain more than 50% of the uncertainties in the MEP-based results.

Keywords: Arctic sea ice; Surface energy budget; Turbulent heat flux; Satellite observation; Reanalysis; Bulk-aerodynamic formula; Maximum entropy production

* Corresponding author. School of Geospatial Engineering and Science, Sun Yat-sen University, Southern Marine Science and Engineering Guangdong Laboratory (Zhuhai), Zhuhai 519082, China.

E-mail address: huifm@mail.sysu.edu.cn (HUI F.-M.).

Peer review under responsibility of National Climate Center (China Meteorological Administration).

<https://doi.org/10.1016/j.accre.2023.04.004>

1674-9278/© 2023 The Authors. Publishing services by Elsevier B.V. on behalf of KeAi Communications Co. Ltd. This is an open access article under the CC BY-NC-ND license (<http://creativecommons.org/licenses/by-nc-nd/4.0/>).

1. Introduction

The rapid warming in the Arctic (known as Arctic amplification) over the past 40 years has been reported based on *in-situ* observations, atmospheric reanalyses, and climate models (IPCC, 2019, 2021), and has also affected the weather and climate at mid-latitudes (Cohen et al., 2014; Zhang et al., 2021a). Simultaneously, Arctic sea ice has experienced rapid changes, with up to a 50% loss in ice thickness, volume, and multi-year ice coverage, as well as late summer/early autumn ice extent (Kacimi and Kwok, 2022; Kwok, 2018). More leads and melt ponds are now being seen, along with an increased number of melt days (Qu et al., 2021; Schröder et al., 2014). These changes in Arctic sea ice have profoundly modified the surface energy budget (Feldl and Merlis, 2021; Riihelä et al., 2021). In turn, the changing surface energy budget has profoundly impacted the climate change in the Arctic, e.g., modulating the sea ice growth and the snow–ice formation (Merkouriadi et al., 2020), and enhancing the Arctic amplification (Dai et al., 2019).

The surface shortwave and longwave radiative fluxes and turbulent fluxes of sensible and latent heat play crucial roles in the surface energy budget of sea ice and atmosphere–ocean interactions. Both satellite observations and atmospheric reanalyses can provide estimates at regional and pan-Arctic scales. Satellite observations are able to characterize radiative fluxes over sea ice, polynyas (Tamura and Ohshima, 2011), and melt ponds (Arndt and Nicolaus, 2014), and can also provide surface information that is applicable for the estimation of turbulent heat fluxes when combined with other information such as data on wind speed (Boisvert et al., 2013) or near-surface air temperature (Qu et al., 2019). To date, however, the uncertainties in the satellite-based surface energy budget components have not been extensively investigated over Arctic sea ice, especially for the turbulent heat fluxes. For the radiative fluxes, errors from the commonly used Clouds and the Earth's Radiant Energy System (CERES) produced by NASA have been widely assessed in recent studies (di Biagio et al., 2021; Lenaerts et al., 2017; Wang et al., 2021), and can be attributed to the imperfect representation of cloud, surface temperature, and albedo over sea ice (Blanchard et al., 2014; di Biagio et al., 2021; van Tricht et al., 2016). However, another commonly used satellite product, the AVHRR Polar Pathfinder-Extended (APP-X) climate data record, have only been evaluated over sea ice using *in-situ* observations from the Surface Heat Budget of the Arctic Ocean (SHEBA) expedition over 20 years ago (Key et al., 2016).

For the turbulent heat fluxes, some studies have used the surface properties (mainly the ice surface temperature) from satellite observations combined with near-surface atmospheric variables from reanalysis products to estimate the turbulent fluxes using the bulk-aerodynamic formula, e.g., over polynyas and leads (Preußner et al., 2016; Qu et al., 2019; Tamura and Ohshima, 2011). Other studies have combined atmospheric variables from satellite observations and reanalysis products (Boisvert et al., 2015a; Boisvert et al., 2013). However, large uncertainties can exist in these estimations due to

errors from the inputs (e.g., the surface and near-surface properties) and the models (e.g., the parameterization schemes). Boisvert et al. (2015b) evaluated the uncertainties in temperature and humidity from the satellite-based Atmospheric Infrared Sounder (AIRS) and ERA-Interim reanalysis products and their derived moisture fluxes, revealing the better performance of the AIRS product. However, no such assessment has yet been made for the other satellite-based turbulent heat flux estimates. In addition to the traditional bulk-aerodynamic formula method, a new turbulent heat flux model has been developed based on maximum entropy production (MEP) theory (Wang and Bras, 2009; Wang et al., 2014) and has been modified and tested over Arctic sea ice in the CICE model (Zhang et al., 2021b). The MEP algorithm is based on the theory of non-equilibrium thermodynamics in the context of information theory and Bayesian probability theory. Given that the MEP model is energy constrained (i.e., the net radiative flux is equal to the sum of the turbulent and conductive heat fluxes over the ice surface) and only surface properties are required, turbulent heat fluxes could be estimated using mainly the ice surface temperature and radiative fluxes from satellite observations, but this has not been achieved to date.

Apart from satellite observations, reanalysis products have been commonly used to study the large-scale Arctic surface energy budget and climate change (Dai et al., 2019; Serreze et al., 2007; You et al., 2021), and have been widely evaluated in terms of the surface properties over sea ice, e.g., ice surface temperature and radiative fluxes (Batak and Müller, 2019; Lenaerts et al., 2017; Wang et al., 2019), as well as turbulent heat fluxes (Graham et al., 2019; Renfrew et al., 2021) and near-surface atmospheric variables (Jakobson et al., 2012; Jonassen et al., 2019; Lüpkes et al., 2010). However, few studies have focused on the inter-comparison of these surface properties based on both satellite observations and reanalysis products. The reliability of satellite products in studying the sea ice surface energy budget (especially for the turbulent heat fluxes) remains poorly understood, compared to reanalysis data.

In this study, we targeted the remote sensing products, i.e., CERES (Doelling et al., 2016) and APP-X (Key, 2016), and the widely used ERA5 atmospheric reanalysis (Hersbach et al., 2018) product to represent the turbulent heat fluxes. Two turbulent flux models (bulk-aerodynamic formula and MEP) were used, in which the key parameters (ice surface temperature and radiative fluxes) were applied from both satellite observations and the ERA5 reanalysis product, while the other parameters were obtained from single sources, i.e., near surface meteorological parameters from ERA5, sea ice concentration from the Advanced Microwave Scanning Radiometer 2 (AMSR2) (Spreen et al., 2008), and snow depth and sea ice thickness from the Pan-Arctic Ice Ocean Modeling and Assimilation System (PIOMAS) (Zhang and Rothrock, 2003). The derived turbulent heat fluxes and the input surface and near surface parameters were compared with *in-situ* observations from the Norwegian Young Sea Ice Cruise (N-ICE2015, January–June 2015) (Granskog et al., 2016; Granskog et al.,

2018), which is one of the few comprehensive field experiments providing simultaneous measurements of surface and near surface parameters over the Arctic sea ice.

The objectives of this study were: 1) to evaluate the bulk-aerodynamic formula and MEP-based turbulent heat flux estimates calculated by applying satellite- and reanalysis-based ice surface temperature and radiative fluxes; 2) to investigate the relationships between the turbulent heat fluxes and the changes in surface and near surface properties; and 3) to quantify the uncertainties in the turbulent heat flux calculations and identify sources of discrepancies. Compared with previous works, e.g., [di Biagio et al. \(2021\)](#), we paid particular attention to the turbulent heat fluxes over Arctic sea ice, instead of radiative fluxes. This study will provide an overview of the dependability of current satellite observations and atmospheric reanalyses in the context of turbulent heat fluxes, which could be referred to for future studies on better understanding the surface energy budget over Arctic sea ice and the thermodynamic interactions between the atmosphere, snow, and sea ice.

2. Data

The data and variables used are listed in [Table 1](#). It should be noted that all the gridded products used were averaged to daily means and resampled onto a 25-km grid in polar stereographic projection.

2.1. Satellite-based ice surface temperature and radiative fluxes

2.1.1. CERES

The CERES synoptic top of atmosphere and surface fluxes and clouds (SYN1deg) product from NASA contains the global radiative fluxes at the surface, top of atmosphere, and various atmospheric layers ([Doelling et al., 2016](#)). These radiative fluxes are derived based on a radiative transfer model using the cloud properties and surface albedo from multi-source satellite observations (e.g. CERES, MODIS, and geostationary imagers) and meteorological parameters from models (e.g. the Goddard Earth Observing System (GEOS)). The CERES-SYN1deg product has a spatial resolution of $1^\circ \times 1^\circ$ (~100 km), with a temporal resolution ranging from 1 h to 1 d. The four components of the radiative fluxes, i.e., shortwave downward flux, shortwave upward flux, longwave downward flux, and longwave upward flux, were expected to have uncertainties less than ± 14 , ± 16 , ± 12 , and $\pm 12 \text{ W m}^{-2}$ in the Arctic, respectively ([Loeb et al., 2018](#)). We selected the daily average ice surface temperature and surface radiative fluxes (all-sky conditions) from the CERES-SYN1deg product.

2.1.2. APP-X

The APP-X climate data record contains twice-daily surface, cloud, and radiative properties in polar regions since 1982 ([Key et al., 2016](#)). The all-sky ice surface temperature and surface radiative fluxes were used. The ice surface temperature is retrieved using the split-window algorithm in clear-sky conditions and is extrapolated to the cloudy areas with an

overall error of $\pm 2.0 \text{ K}$ over Arctic sea ice. The surface radiative fluxes are computed based on a neural network trained to simulate a radiative transfer model ([Key and Schweiger, 1998](#)), using surface and cloud properties from the AVHRR product and meteorological parameters from the Modern-Era Retrospective Analysis for Research and Applications (MERRA) reanalysis product. In the Arctic, uncertainties of the four components of radiative fluxes were expected to be less than ± 34 , ± 27 , ± 22 , and $\pm 9 \text{ W m}^{-2}$, respectively ([Key et al., 2016](#)). The APP-X climate data record was acquired from the National Centers for Environmental Information (NCEI) of NOAA ([Key, 2016](#)).

2.2. ERA5 reanalysis

ERA5, from the European Centre for Medium-Range Weather Forecasts (ECMWF), is one of the most accurate reanalysis datasets for the Arctic ([Graham et al., 2019](#)). The ERA5 hourly data with spatial resolution of $0.25^\circ \times 0.25^\circ$ (~31 km) were acquired from the Climate Data Store (CDS) of the ECMWF ([Hersbach et al., 2018](#)). The skin temperature, radiative fluxes, and the near surface meteorological parameters (10-m wind speed, 2-m air temperature, and 2-m dew point) were selected as some of the inputs in turbulent flux calculations. ERA5 turbulent heat fluxes were also used for comparison with the satellite-based estimates and *in-situ* observations. In the ECMWF Integrated Forecast System (IFS) which provides model forecasts to produce ERA5, the bulk-aerodynamic algorithm is used for the surface turbulent flux parameterizations, applying with surface roughness lengths and stability functions specific for various surface types (land, ocean or sea ice) ([ECMWF, 2021](#)). According to [Graham et al. \(2019\)](#), uncertainties in the near surface air temperature and 10-m wind speed were $\pm 2.7 \text{ K}$ and $\pm 1.1 \text{ m s}^{-1}$, respectively. Uncertainties in the net shortwave radiative fluxes, net longwave radiative fluxes, and the sensible heat fluxes were ± 18 , ± 34 , $\pm 16 \text{ W m}^{-2}$, respectively.

2.3. Auxiliary data

2.3.1. AMSR2 sea ice concentration

Sea ice concentration data were used for the turbulent flux calculation in the bulk-aerodynamic formula model. The daily Arctic sea ice concentration from the AMSR2 brightness temperature obtained using the Arctic Radiation and Turbulence Interaction Study (ARTIST) sea ice (ASI) algorithm ([Spreen et al., 2008](#)) was selected, considering its relatively high spatial resolution (6.25 km). The uncertainties were expected to be less than $\pm 10\%$ when sea ice concentration is over 65% ([Spreen et al., 2008](#)). The ASI sea ice concentration data were acquired from the University of Bremen (<https://seaice.uni-bremen.de/sea-ice-concentration/amsre-amsr2/>). Accessed on Mar. 30, 2022).

2.3.2. PIOMAS snow depth and sea ice thickness

Daily snow depth and sea ice thickness data are indispensable parameters in the MEP approach. Given that the

Table 1
Data sources and variables used.

Type	Data	Variable	Usage in BF/MEP ^a	Spatial resolution	Temporal resolution	Uncertainty	Reference
Satellite-based IST ^a and radiative fluxes	CERES-SYN1deg	IST Radiative fluxes ^b	BF, MEP MEP	~100 km	Daily average (1 h)	— 14 W m ⁻² , 16 W m ⁻² , 12 W m ⁻² , 12 W m ⁻²	Doelling et al. (2016); Loeb et al. (2018)
	APP-X	IST Radiative fluxes ^b	BF, MEP MEP	25 km	Daily average (Twice a day)	2 K 34 W m ⁻² , 22 W m ⁻² , 27 W m ⁻² , 9 W m ⁻²	Key (2016); Key et al. (2016)
Reanalysis-based IST and energy fluxes	ERA5	IST Radiative fluxes ^b	BF, MEP MEP	~25 km	Daily average (1 h)	2.7 K 18 W m ⁻² for net shortwave, 34 W m ⁻² for net longwave 16 W m ⁻² for sensible flux	Hersbach et al. (2018); Graham et al. (2019)
Auxiliary data	ASI-AMSR2	Turbulent heat fluxes ^c	—	6.25 km	Daily	10%	Spren et al. (2008)
	ERA5	Sea ice concentration Near surface parameters ^d	BF BF	~25 km	Daily average	2.7 K, —, 1.1 m s ⁻¹	Hersbach et al. (2018); Graham et al. (2019)
	PIOMAS	Snow depth, ice thickness	MEP	~22 km	Daily	0.8 m for ice thickness	Zhang and Rothrock (2003); Stroeve et al. (2014)
<i>In-situ</i> data	N-ICE2015	Near surface parameters ^d	—	point	1 min	0.3 °C, 2.4%, 0.2 m s ⁻¹	Hudson et al. (2015);
		Radiative fluxes ^b	—	point	30 min	5 W m ⁻²	Hudson et al. (2016);
		Turbulent heat fluxes ^c	—	point	30 min	2 W m ⁻² , 0.2 W m ⁻²	Walden et al. (2017b);
		Snow depth, ice thickness	—	point	Daily	0.06 m, 0.07 m	Itkin et al. (2015)

Abbreviations: IST, ice surface temperature; BF, bulk-aerodynamic formula; MEP, maximum entropy production.

^b Including shortwave downward, shortwave upward, longwave downward, and longwave upward component.

^c Including sensible and latent heat fluxes.

^d Including 2-m air temperature, 2-m dew point temperature (for ERA5 only), 2-m relative humidity (for N-ICE2015 only), and 10-m wind speed.

daily Arctic sea ice thickness is still not available from satellite observations, the snow depth and ice thickness were instead simulated by applying the PIOMAS product (Zhang and Rothrock, 2003). Various assessments of the PIOMAS simulation have confirmed its ability in the reconstruction of the Arctic sea ice volume field (Schweiger et al., 2011; Stroeve et al., 2014) with uncertainties of ice thickness less than ± 0.8 m. The daily PIOMAS product was obtained from the Polar Science Center (PSC) at the University of Washington (http://psc.apl.uw.edu/research/projects/arctic-sea-ice-volume-anomaly/data/model_grid, access on Mar. 2022). The mean spatial resolution of the PIOMAS data is approximately 22 km.

2.4. In-situ observations

The N-ICE2015 *in-situ* observations were used for the validation. The N-ICE2015 drifting ice station field campaign consisted of four separate legs. Two took place during the winter season (15 Jan.–21 Feb. and 24 Feb.–19 Mar.), one was in spring (18 Apr.–5 Jun.), and the other was in early summer (7–22 Jun.) (Granskog et al., 2018). The trajectories of the four legs and the sea ice concentration during the drifting period are shown in Fig. 1.

The 2-m air temperature, relative humidity, and 10-m wind speed were measured at 1-min intervals with uncertainties of ± 0.3 °C, $\pm 2.4\%$, and ± 0.2 m s⁻¹, respectively (Cohen et al., 2017). The shortwave downward (R_{SWD})/upward (R_{SWU}),

and longwave downward (R_{LWD})/upward (R_{LWU}) radiative fluxes were measured every 30 min with uncertainties less than ± 5 W m⁻² (Walden et al., 2017a). The surface temperature of snow/ice (T_{skin}) was estimated using R_{LWD} and R_{LWU} by:

$$T_{skin} = \left[\frac{R_{LWU} - (1 - \epsilon_s)R_{LWD}}{\epsilon_s \sigma} \right]^{\frac{1}{4}} \tag{1}$$

where σ is Planck's constant and ϵ_s is the emissivity of snow. Here, ϵ_s is assumed to be 0.99, according to Walden et al. (2017a). The sensible and latent heat fluxes were measured using a sonic anemometer in a half-hourly sampling interval with uncertainties of ± 2 W m⁻² and ± 0.2 W m⁻², respectively. More details of the surface meteorology and energy flux measurements and components are given in Cohen et al. (2017) and Walden et al. (2017a). The daily snow depth and sea ice thickness were estimated using the Sea Ice Mass Balance for the Arctic (SIMBA) buoys set up around the ice station (within 1 km) on each floe (Rösel et al., 2018). For each floe drift trajectory, the snow depth and sea ice thickness were averaged from all the buoy records (five buoys for Drift 1, two buoys for Drift 2, and one buoy for Drift 3) with average uncertainties of ± 0.06 m and ± 0.07 m, respectively. The N-ICE2015 observations were acquired from the Norwegian Polar Data Centre (NPDC) (Hudson et al., 2015, 2016; Itkin et al., 2015; Walden et al., 2017b).

3. Methods

3.1. Turbulent heat flux models

3.1.1. Bulk-aerodynamic formula and SHEBA parameterization

The turbulent fluxes of the surface sensible heat (H_s) and latent heat (H_l) were estimated based on Monin-Obukhov similarity theory (Monin and Obukhov, 1954). The bulk-aerodynamic formula characterizes H_s and H_l as:

$$H_s = \rho_a c_p C_H S_r (T_s - T_r) \tag{2}$$

$$H_l = \rho_a L_v C_E S_r (Q_s - Q_r) \tag{3}$$

where ρ_a is the air density; c_p is the specific heat at constant pressure; L_v is the latent heat of vaporization; S_r , T_r , and Q_r are the effective wind speed, air potential temperature, and specific humidity at reference height r ($r = 2$ m), respectively; and T_s and Q_s are the surface skin potential temperature and specific humidity, respectively. S_r depends on the wind speed at a 10-m height (the ERA5 output includes air temperature and humidity at the height of 2 m, but wind speed at the height of 10 m), and can be calculated using the wind profile equation (Ray et al., 2006). C_H and C_E are the transfer coefficients of sensible heat and latent heat, respectively, which depend on the roughness length for the momentum (z_0) and heat/moisture (z_T/z_Q) and the stability function for the momentum (ψ_m) and heat/moisture (ψ_s).

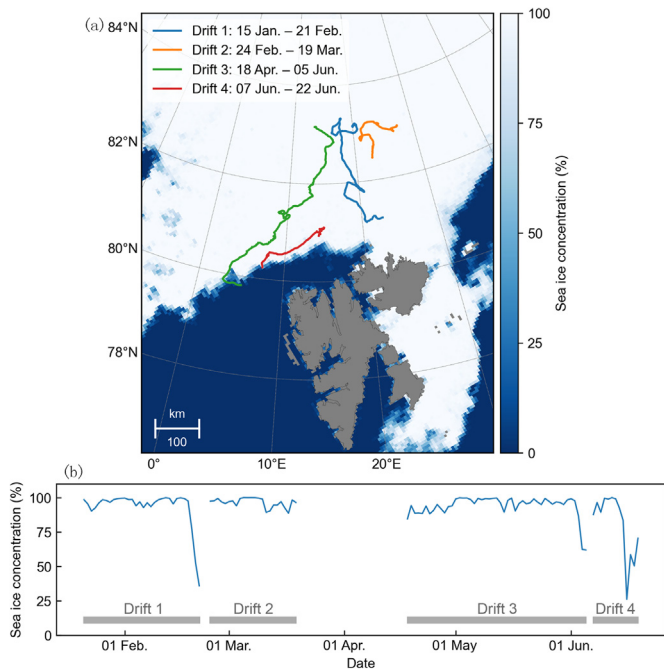


Fig. 1. (a) Drift trajectories and periods of the four N-ICE2015 floe drifts north of Svalbard (The sea ice concentration shown on the map is from June 22, 2015. Land areas are masked in grey), and (b) time series of sea ice concentration during the N-ICE2015 drifts, obtained from the ASI-AMSR2 product (The daily sea ice concentration is from the pixel nearest to the daily average position of the N-ICE2015 drifting ice station).

Table 2
Input combinations for the bulk-aerodynamic formula/SHEBA model and MEP model.

Method	Group	Ice surface temperature	Surface parameter ^a	Sea ice concentration	Radiative fluxes	Snow depth and ice thickness
Bulk-formula	B1	ERA5	ERA5	ASI-AMSR2	—	—
	B2	CERES	ERA5	ASI-AMSR2	—	—
	B3	APP-X	ERA5	ASI-AMSR2	—	—
MEP	M1	ERA5	—	—	ERA5	PIOMAS
	M2	CERES	—	—	CERES	PIOMAS
	M3	APP-X	—	—	APP-X	PIOMAS

^a Including 2-m air temperature, 2-m dew point temperature, and 10-m wind speed.

For z_0 , we applied the parameterization schemes of [Andreas et al. \(2010a, b\)](#), characterizing z_0 in the marginal ice zone and in compact ice conditions according to SHEBA field observations. The scalar roughness lengths z_T/z_Q were calculated from z_0 according to [Andreas \(1987\)](#). The parameterization of S_r depends on the stratification, and for the stability functions ψ_m and ψ_s , we applied the forms from [Grachev et al. \(2007\)](#) in stable stratification and those from [Paulson \(1970\)](#) in unstable stratification. For S_r , we selected the model produced by [Jordan et al. \(1999\)](#) for stable stratification and the model produced by [Fairall et al. \(1996\)](#) for unstable stratification (see the Appendix). The turbulent flux into the ice surface is defined as positive (heating the surface), and that leaving the surface as negative (cooling the surface).

The input combinations for the bulk-aerodynamic formula method are given in [Table 2](#). It should be noted that, for the gridded data, T_s (Q_s) in [Eq. 2](#) is a combination of the surface skin potential temperature (specific humidity) from ice (T_{ice} , Q_{ice}) and open water (T_{ow} , Q_{ow}):

$$T_s = C_i T_{ice} + T_{ow} (1 - C_i) \quad (4)$$

$$Q_s = C_i Q_{ice} + Q_{ow} (1 - C_i) \quad (5)$$

where C_i is the sea ice concentration from AMSR2. Given $T_{ow} = 271.35$ K (-1.8 °C), T_{ice} can be estimated using T_s and C_i from the satellite observations or reanalysis product. Assuming that air is always saturated at the surface of ice or water, Q_{ice} and Q_{ow} can be derived from T_{ice} and T_{ow} (Eqs. A16–A17). Similarly, Q_r can be derived from the dew point temperature from ERA5.

3.1.2. Maximum entropy production approach

The MEP algorithm provides an analytical solution for the sensible H_s , latent H_l , and conductive heat flux H_c of the sea ice surface, as a function of net surface radiation (R_{net}) and T_s ([Wang et al., 2014](#)). The dissipation (D) of the heat fluxes is expressed as:

$$D(H_s, H_l, H_c) = \frac{2H_s^2}{I_s} + \frac{2H_l^2}{I_l} + \frac{2(R_{net} + H_c)^2}{I_c} \quad (6)$$

where R_{net} is the sum of the net shortwave (R_{NSW}) and long-wave radiative fluxes (R_{NLW}); and I_s , I_l , and I_c are the thermal inertia of the sensible, latent, and conductive heat fluxes of the ice surface, respectively. The thermal inertia I_s is defined as

$I_s = \rho_a c_p \sqrt{C_1 k z u_*'}$, where u_*' is the extreme solution of u_* based on Monin-Obukhov similarity theory ([Wang and Bras, 2009](#)). The effect of wind speed on the turbulent fluxes is implicitly included through the formulation of I_s . I_c is in analogy with the thermal conductivity of sea ice or snow. Given R_{net} and T_s as inputs, the turbulent and conductive heat fluxes can be derived by minimizing the dissipation D under the constraint of the surface energy balance ([Wang and Bras, 2011](#); [Wang and Bras, 2009](#)) (see the Appendix for details).

We adopted the modification of R_{NSW} in the MEP model given by [Zhang et al. \(2021b\)](#), where the shortwave radiation absorbed in the surface layer of snow or ice ($R_{NSW,a}$) is defined as:

$$R_{NSW,a} = R_{NSW} - R_{NSW} e^{-(e_s h_s + e_i h_i)} \quad (7)$$

where $R_{NSW} e^{-(e_s h_s + e_i h_i)}$ represents the amount of shortwave radiation transmitted through the ice or snow surface. e_s and e_i are the extinction coefficients for snow and ice, respectively; and h_s and h_i are the thickness of the snow and sea ice, respectively. The thermal inertia I_c was also modified as $I_c = k_s k_i / (k_s h_i + k_i h_s) \times 10^3$, where k_s and k_i are, respectively, the thermal conductivity of snow and sea ice. $R_{NSW,a}$ was used to calculate R_{net} instead of R_{NSW} . The input combinations for the MEP model are listed in [Table 2](#). For clarity, the primary variables in the bulk-formula and MEP model and their symbols are summarized in [Table 3](#).

3.2. Collocation and comparison of the N-ICE2015 measurements and gridded data

The surface and atmospheric parameters ([Table 1](#)) and the estimated turbulent fluxes ([Table 2](#)) from the gridded satellite or reanalysis data were co-located and compared with the N-ICE2015 observations. To compare the gridded data (a mixture of sea ice and open water) with the *in-situ* point measurements (footprint on the sea ice), a sea ice concentration (SIC) mosaic method ([di Biagio et al., 2021](#)) was used to estimate the N-ICE2015-based gridded observations ($X_{grid,N-ICE2015}$) for the surface parameters, i.e., T_s , h_s , h_i , R_{SWU} , R_{LWU} , H_s , and H_l :

$$X_{grid,N-ICE2015} = C_i X_{N-ICE2015} + (1 - C_i) X_{ow} \quad (8)$$

where X refers to each surface parameter, $X_{N-ICE2015}$ is the original N-ICE2015 observation, X_{ow} is the assumed surface

Table 3
Primary variables used in the bulk-formula and MEP model and their symbols.

Variable	Symbol	Bulk-formula	MEP model
Air density	ρ_a	✓	✓
Specific heat	c_p	✓	✓
Latent heat of evaporation	L_v	✓	✓
Near surface wind speed	U_r	✓	
Surface skin temperature	T_s	✓	✓
Near surface air temperature	T_r	✓	
Surface specific humidity	Q_s	✓	
Near surface specific humidity	Q_r	✓	
Transfer coefficient of sensible (latent) heat	C_H (C_E)	✓	
Net shortwave (longwave) radiative flux	R_{NSW} (R_{NLW})		✓
Snow depth over sea ice	h_s		✓
Sea ice thickness	h_i		✓

parameter for open water, and C_i is the sea ice concentration from AMSR2. For X_{ow} , T_s is assumed to be 271.35 K for open water, and h_s and h_i are zero. R_{SWU} for open water was calculated as $A_{ow} \times R_{SWD,N-ICE2015}$, where $A_{ow} = 0.08$ is the surface albedo of open water. R_{LWU} was estimated using the Stefan Boltzmann law, and the emissivity of open water was assumed to be 0.99. H_s and H_i for open water were derived using the bulk-aerodynamic formula (Eqs. 2 and 3). For simplicity, the near-surface wind speed and air temperature over the open water and sea ice were assumed to be the same, though this is not always the case especially when the open water fraction is around 50% (Vihma, 1995; Vihma et al., 1998). The scalar transfer coefficients at a 2-m height were assumed to be 2.0×10^{-3} , as the commonly used values over open water in the marginal ice zone as well as polynya and lead areas range from 1.5×10^{-3} to 3.0×10^{-3} (Adams et al., 2012; Lüpkes et al., 2012; Maykut, 1982; Pond et al., 1974). The N-ICE2015-based gridded observations were used as a reference for all the evaluations in this paper, unless otherwise stated.

The uncertainties of the SIC-adjusted N-ICE2015 gridded observations (σ_X) were calculated using the error propagation equation given as

$$\sigma_X^2 = \sum \sigma_x^2 \left(\frac{dX}{dx} \right)^2 \tag{9}$$

where σ_x is the error of each variable, and $\frac{dX}{dx}$ is the derivative of the estimated result with respect to each variable. Assuming that the original N-ICE2015 observations represent the surface conditions over sea ice, then the errors mainly come from sea ice

concentration (C_i) and the estimated surface parameters of open water ($T_s, h_s, h_i, R_{SWU}, R_{LWU}, H_s,$ and H_i). The estimated error of the AMSR2 sea ice concentration is less than 10% when the concentration is above 65% (Spren et al., 2008). The error of T_s over open water can be expected to be less than -1.8 K since the highest air temperature during the drifting period was around 0°C . For R_{SWU} , the albedo of the sea surface ranges from 0.06 to 0.15 for the N-ICE2015 positions, and its uncertainty is assumed to be 0.07, as given by di Biagio et al. (2021). For R_{LWU} , given that the emissivity of the ocean surface is 0.925, on average, over the thermal infrared domain (Feldman et al., 2014), the error is assumed to be less than 0.065. For H_s and H_i , the transfer coefficients can be expected to have a bias of less than 1.0×10^{-3} , according to the widely used values over open water in the marginal ice zone, polynya, and lead areas (1.5×10^{-3} – 3.0×10^{-3}). The average values of the surface variables from the raw N-ICE2015 point observations, the N-ICE2015 gridded observations, and the corresponding uncertainties are listed in Table 4.

The N-ICE2015 gridded observations were averaged into daily means and collocated with the nearest pixel in the gridded satellite or reanalysis data. The following statistical indices were calculated for the comparisons: mean value, correlation coefficient (r), mean bias (MB), and root-mean-square error ($RMSE$).

4. Results

4.1. Turbulent heat fluxes from the bulk-aerodynamic formula and MEP

The turbulent heat fluxes were estimated using the bulk-aerodynamic formula and MEP model with various combinations of input data. For the results based on the bulk-, B2 and B3), the ice surface temperature was taken from ERA5, CERES and APP-X, respectively. For the MEP-based estimates (M1, M2 and M3), both ice surface temperature and radiative fluxes were from ERA5, CERES and APP-X, respectively. Other input parameters were the same in B1–B3 or M1–M3 (Table 2). The time series of the turbulent heat flux estimates based on bulk-formula and MEP are shown in Fig. 2, compared with the N-ICE2015 observations and ERA5 reanalysis products. Sea ice concentration from AMSR2 is also shown. The seasonal statistics of the derived turbulent heat fluxes are given in Table 5.

In the winter months (February and March), the sensible heat flux ($<25 \text{ W m}^{-2}$) and latent heat flux (close to 0) are relatively stable when the sea ice pack is consolidated ($\sim 100\%$

Table 4
Mean values of the variables from the N-ICE2015 point observations, N-ICE2015-based gridded observations, and the corresponding uncertainties.

N-ICE2015 observations	T_s (K)	R_{SWU} (W m^{-2})	R_{LWU} (W m^{-2})	H_s (W m^{-2})	H_i (W m^{-2})	h_s (m)	h_i (m)
Original	258.6	177.4	256.7	0.9	−0.3	0.5	1.4
Adjusted	259.1	164.7	258.4	−6.9	−3.1	0.5	1.3
Uncertainty	1.4	5.9	3.8	10.7	4.6	0.03	0.08

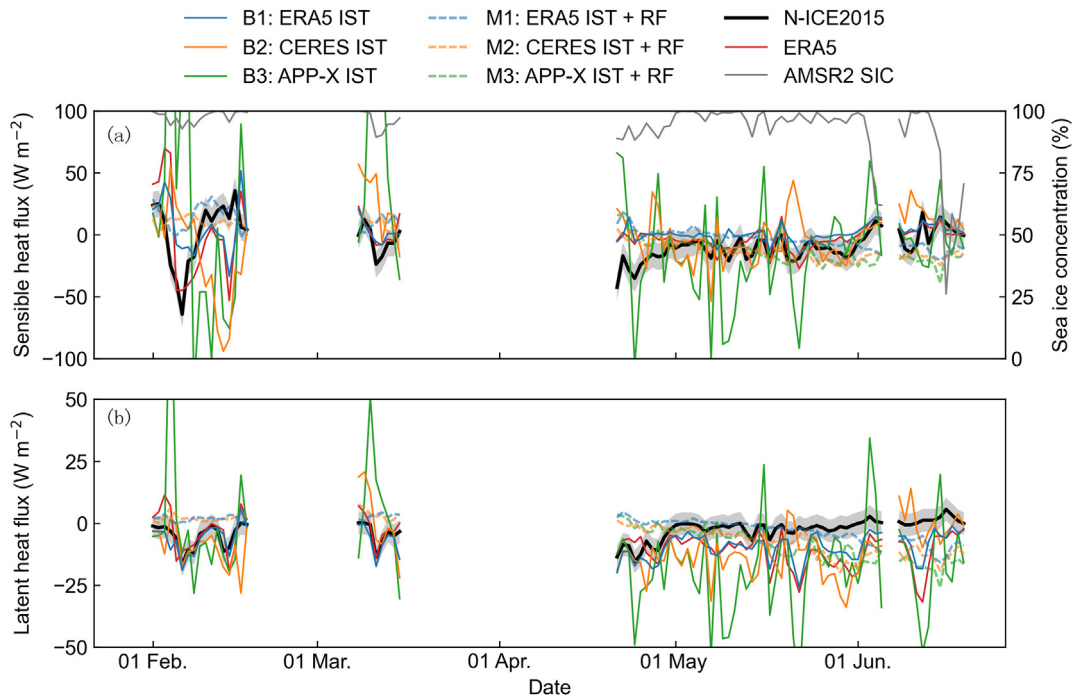


Fig. 2. Time series of (a) the surface sensible heat flux and (b) latent heat flux from the *in-situ* measurements, ERA5 reanalysis, estimates based on the bulk-aerodynamic formula (solid line) and MEP (dashed line) using ice surface temperature and radiative fluxes from ERA5, CERES, and APP-X (The uncertainties of the gridded *in-situ* measurements are shaded in grey).

sea ice concentration). Once ~10% open water is exposed, upward sensible heat fluxes over 25 W m^{-2} and latent heat fluxes over 10 W m^{-2} (cooling the surface) are detected by the N-ICE2015 observations. The two reanalysis-based estimates (B1 and ERA5) capture the trend and magnitude of the sensible heat flux variations ($r > 0.2$ and $RMSE < 30 \text{ W m}^{-2}$). For the two satellite-based results, B2 agrees better with *in-situ* observations with $RMSE$ of $\sim 55 \text{ W m}^{-2}$ whereas B3 shows great fluctuations. The variation of latent heat flux is well captured by B1, B2 and ERA5 data, among which B1 shows

the highest agreement with *in-situ* observations ($r > 0.8$ and $RMSE < 5 \text{ W m}^{-2}$). For the MEP-based estimates, M1 and M2 could capture the trend of turbulent fluxes when they are in positive values (heating the surface) but fail in the negative cases (cooling the surface). Nevertheless, both M1 and M2 show relatively small $RMSE$ s for sensible heat ($< 26 \text{ W m}^{-2}$) and latent heat fluxes ($< 10 \text{ W m}^{-2}$).

During the spring (April and May), strong turbulent heat exchanges are observed in N-ICE2015 in the late April (upward sensible heat flux near 50 W m^{-2} and latent heat flux $>$

Table 5
Statistics of the bulk-aerodynamic formula based (B1–B3) and MEP-based turbulent heat fluxes (M1–M3) and ERA5 reanalysis, compared with the N-ICE2015 observations.

Variable	Group	Total (82 d)				Winter (Jan.–Mar., 26 d)				Spring (Apr.–May, 39 d)				Summer (June, 17 d)			
		Mean	r	MB	RMSE	Mean	r	MB	RMSE	Mean	r	MB	RMSE	Mean	r	MB	RMSE
Sensible heat flux (W m^{-2})	Obs	-6.9	—	—	—	-0.6	—	—	—	-14.4	—	—	—	1.6	—	—	—
	B1	2.0	0.35	8.9	18.3	4.3	0.25	4.9	24.9	-1.5	0.11	12.9	16.1	6.8	0.67	5.2	8.5
	B2	-0.5	-0.24	6.4	36.2	0.4	-0.44	1.0	55.4	-6.1	-0.28	8.3	24.9	11.6	-0.20	10.1	17.3
	B3	2.4	-0.18	9.3	76.0	36.8	-0.53	37.4	125.0	-19.1	0.12	-4.8	41.3	1.7	0.29	0.2	22.4
	M1	1.4	0.17	8.3	19.8	13.7	0.49	14.4	23.8	-0.9	-0.29	13.5	17.9	-12.0	-0.48	-13.5	17.6
	M2	-6.3	0.08	0.6	19.5	10.1	-0.34	10.8	25.9	-12.3	-0.25	2.1	12.9	-17.2	-0.21	-18.8	21.3
	M3	-13.4	-0.54	-3.7	19.1	—	—	—	—	-10.3	-0.38	4.2	15.9	-20.7	-0.25	-22.2	25.1
ERA5	-1.5	0.43	5.4	19.5	-1.6	0.40	2.2	30.1	-6.2	0.15	8.2	13.4	5.0	0.63	3.4	7.7	
Latent heat flux (W m^{-2})	Obs	-3.1	—	—	—	-4.8	—	—	—	-3.9	—	—	—	1.1	—	—	—
	B1	-8.6	0.55	-5.5	7.4	-6.3	0.82	-1.6	3.7	-10.9	0.57	-7.0	8.2	-6.8	0.28	-7.9	9.3
	B2	-9.7	0.27	-6.5	12.2	-6.0	0.44	-1.2	10.1	-14.7	0.01	-10.8	14.3	-3.2	-0.14	-4.3	9.4
	B3	-12.3	0.07	-9.2	25.0	1.0	0.19	5.8	26.7	-20.4	0.11	-16.6	23.6	-13.3	0.18	-14.4	25.5
	M1	-1.7	-0.54	-1.5	8.1	2.1	-0.04	6.8	8.4	-0.9	-0.41	2.9	6.1	-9.2	-0.55	-10.3	11.1
	M2	-4.8	-0.47	-1.7	9.9	2.4	0.20	7.2	8.6	-6.1	-0.44	-2.2	8.1	-12.9	-0.24	-14.0	14.4
	M3	-9.1	-0.64	-6.7	12.0	—	—	—	—	-5.9	-0.48	-2.0	8.2	-16.4	-0.03	-17.6	17.9
ERA5	-8.6	0.14	-5.5	10.3	-2.5	0.74	2.2	5.6	-11.5	0.02	-7.7	10.4	-11.0	0.31	-12.1	14.6	

10 W m^{-2}), along with relative low sea ice concentration (<90%). Since then small fluctuations appear with sensible heat flux ranging from -20 to 0 W m^{-2} and latent heat flux close to 0. For the estimates based on the bulk-formula, the two reanalysis-based results (B1 and ERA5) generally capture the trend of sensible heat in May with *RMSE* around 15 W m^{-2} . The satellite-based B2 and B3 show large fluctuations while B2 has a lower *RMSE* of 25 W m^{-2} . All the results overestimate the upward latent heat flux by $7\text{--}17 \text{ W m}^{-2}$, while B1 agrees much better with the *in-situ* observations with *r* of 0.6. In contrast, all the MEP-based estimates show relatively stable declining trends throughout the spring. Either reanalysis-based or satellite-based result performs similarly with *RMSEs* less than 18 W m^{-2} for sensible heat flux and 9 W m^{-2} for latent heat flux.

In the early summer, the melt of sea ice advances with fast-changing sea ice concentration and air temperature. The sensible heat flux starts to vary in direction and amplitude (-10 to 15 W m^{-2}). Events of downward (positive) latent heat flux of up to 5 W m^{-2} occurred in N-ICE2015 observations in summer, associated with transport of warm, moist airmasses to over the colder sea ice (indicated by the wind speed, temperature and specific humidity shown in Fig. 4). All the estimates based on the bulk-formula overestimate the downward sensible heat flux by $0\text{--}10 \text{ W m}^{-2}$, whereas the trends and magnitudes are better captured by the reanalysis-based results (B1 and ERA5), with *r* over 0.6 and *RMSE* less than 9 W m^{-2} . The latent heat fluxes are estimated in the wrong direction for all the estimates based on bulk-formula, among which the reanalysis-based B1 and satellite-based B2 show relatively small *RMSE* of 9 W m^{-2} . In comparison, the MEP-based results show an opposite direction of turbulent heat fluxes for most of the time (cooling the surface), with larger biases and *RMSEs* for all estimates (M1, M2, and M3).

The overall performance of these estimates is also evaluated (Fig. 3 and Table 5). In summary, the reanalysis-based B1 outperforms the two satellite-based B2 and B3 with higher *r* and lower *RMSE* (18 W m^{-2} for sensible heat flux and 7 W m^{-2} for latent heat flux), using either bulk-formula or MEP model. The CERES-based B2 performs better than the APP-X-based B3 (e.g., 36 vs. 76 W m^{-2} for *RMSE* from the bulk-formula based results). Though MEP cannot well capture the trend of the turbulent heat flux variations, it has comparable performance (in terms of *RMSE*) to the bulk-formula and reanalysis-based estimates (B1 and ERA5) when using the satellite-based ice surface temperature and radiative fluxes (M2 and M3). Compared to ERA5, the *RMSEs* in B1 (using ERA5 as inputs) are reduced by 1 W m^{-2} for sensible heat flux and 3 W m^{-2} for latent heat flux, which likely leads to the improvement of the SHEBA parameterization scheme relative to the ERA5 ones.

4.2. Drivers of the turbulent heat flux variations

The surface and near surface parameters shown in Fig. 4 depict the overall weather conditions (within 25 km grid cell) during the N-ICE2015 period. Given the different performance of the turbulent heat flux estimates (B1–B3 and M1–M3) in

Section 4.1, it is important to analyze their linkages to the surface and near surface parameters. We selected three periods during the N-ICE2015 with different weather conditions for case studies. In addition, the correlation coefficient between the turbulent heat fluxes and the surface and near surface parameters were calculated for the entire N-ICE2015 period (Table 6).

Case 1. represents a rapid surface warming process within a week during the cold winter condition. A rapid increase of surface and near surface temperature (over 20 K) is observed with the invasion of the warm and humid air mass (with 10-m wind speed up to 12 m s^{-1}). Partial opening of the sea ice cover (sea ice concentration below 95%) leads to a large temperature gradient between air and surface (near 5 K). Thus, a large downward turbulent heat flux (up to 90 W m^{-2}) is observed as a result of the large air–ice temperature gradient and strong wind. The near zero net longwave radiative flux indicates a balance between the upward longwave radiation from the ice surface and downward radiation from the low-level clouds. ERA5 well delineates the changes of surface and near surface parameters and hence the changes in turbulent heat flux estimates (ERA5 and B1). The surface temperature and gradient are better captured by CERES than APP-X (Fig. 4f and g), thus CERES-based turbulent flux (B2) outperforms APP-X-based one (B3). From the point of view of surface energy budget, ERA5 is in excellent agreement with the *in-situ* observations in net radiation compared to CERES, while the ERA5-based estimates (M1) fail to capture the rapid change in turbulent heat flux, instead showing an opposite trend to the net radiative flux. It results from the energy-constrained MEP model, which keeps the balance between the radiative, turbulent and conductive fluxes. However, during the transient weather events there is not necessarily the balance, especially when phase changes occur (freezing in the open leads in this case).

Case 2. shows a fast cooling process after the continuous surface warming in the early March. The relatively low values of temperature (<250 K), specific humidity (near zero) and wind speed (< 5 m s^{-1}) indicate a dry and cold weather condition along with strong radiative cooling ($\sim 50 \text{ W m}^{-2}$). However, a strong turbulent heat release ($\sim 60 \text{ W m}^{-2}$) still occurs when the sea ice concentration decreases below 95% with a negative air–surface temperature gradient. In this case, ERA5 captures the drop of air and surface temperature with an overestimation of $\sim 10 \text{ K}$. CERES is comparable with ERA5 in surface temperature while APP-X agrees well with the *in-situ* observations. Nevertheless, the bias in the temperature gradient is mitigated for ERA5 and CERES due to similar biases in air and surface temperature but appears large for APP-X ($>10 \text{ K}$). This leads to a better agreement of turbulent heat flux from ERA5, ERA5-based B1 and CERES-based B2 with the N-ICE2015 observations. The MEP-based M1 and M2 still show deficiencies in delineating the ice surface energy budget in the cases with rapid surface cooling and heterogeneous surface conditions.

Case 3. represents a stable weather condition during early spring. The surface temperature remains near 260 K with moderate wind speed and low humidity. The net solar radiation

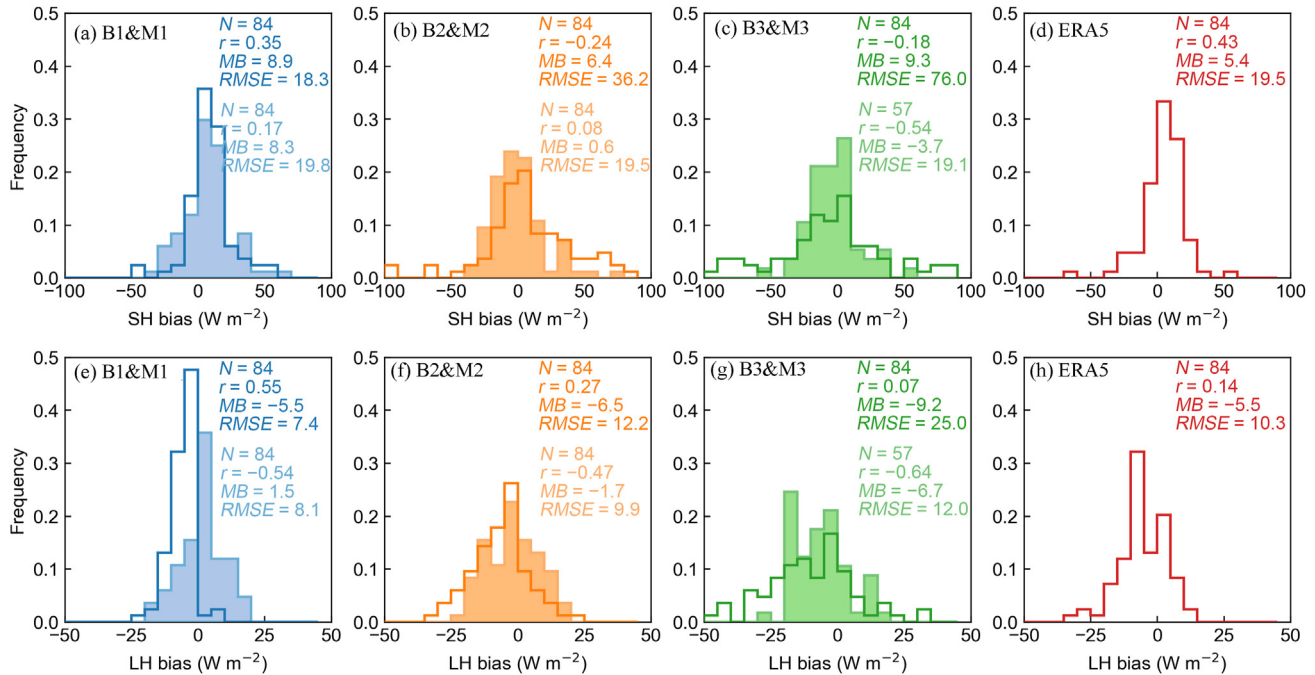


Fig. 3. Histograms of (a–d) the sensible heat (SH) flux bias and (e–h) latent heat (LH) flux bias of the estimates based on the bulk-aerodynamic formula (solid lines) and MEP (shades), compared with the N-ICE2015 measurements (The bin size is 10 W m^{-2} for the sensible heat flux bias and 5 W m^{-2} for the latent heat flux bias).

gradually increases to $\sim 50 \text{ W m}^{-2}$ while the net radiation remains close to zero. The turbulent heat exchange between the air and ice surface is weak ($< 20 \text{ W m}^{-2}$) over the compact ice cover (sea ice concentration $> 95\%$). The turbulent heat fluxes are correctly estimated by ERA5 and B1 but overestimated by B2 and B3 (up to 40 W m^{-2} and 100 W m^{-2}) due to an overestimation of surface temperature for CERES and APP-X (up to 6 K and 9 K, respectively). Though the net radiative flux is slightly overestimated in CERES and APP-X, compared to ERA5, the MEP-based turbulent heat fluxes (M1, M2 and M3) agree quite well with the *in-situ* observations.

We also calculated the overall correlation coefficients between the turbulent heat fluxes and surface/near surface parameters from *in-situ* observations, ERA5 reanalysis and satellite estimates (Table 6). Generally, turbulent heat flux from the *in-situ* observations and bulk-formula based estimates (ERA5 and B1–B3) show significant correlation with the temperature gradients ($r > 0.7$) while the MEP-based results (M1–M3) are strongly correlated with the net surface radiation ($r < -0.9$) and some other surface parameters (e.g., surface temperature and humidity). The correlation analysis and the case studies suggest that the turbulent heat fluxes based on bulk aerodynamic formula is temperature gradient-driven while those from MEP relies heavily on the radiation budget over sea ice. These characteristics are observed for both atmospheric reanalysis and satellite-based estimates.

4.3. Uncertainties of the satellite-based turbulent heat flux estimates

It is of interest to quantify the uncertainties of the bulk-aerodynamic formula based and MEP-based turbulent flux

estimates (B1–B3 and M1–M3). The major factors in the bulk-aerodynamic formula method are ρ_a , c_p , L_v , U_{10m} , T_s , T_{2m} (or Q_{2m} , Q_s), C_H , and C_E . For the MEP model, R_{net} , h_s , and h_i are considered, in addition to ρ_a , c_p , L_v , and T_s . The errors of ρ_a , c_p , and L_v are assumed to be 10%, 0.1%, and 15% (given that the surface air temperature varies from 250 to 300 K), respectively. The surface and near surface parameters from reanalysis data and satellite product are validated against the N-ICE2015 observations (Fig. 4). The transfer coefficients derived in B1–B3 are compared with those from using the same bulk-formula parameterizations but the N-ICE2015 observations as inputs. Assuming that the errors of the variables are uncorrelated, the error propagation functions (Eq. 8) can be used to calculate the uncertainties of the estimated turbulent heat fluxes (σ_H). The contributions to the total uncertainties for each variable $\sigma_x \left(\frac{dH}{dx} \right)$ are also calculated in percentage. The overall uncertainties of the turbulent heat flux estimates, the mean error and contribution of each input variable to the uncertainties are listed in Table 7.

In general, the estimated uncertainties (σ_{H_s} and σ_{H_i}) for the three estimates based on the bulk-aerodynamic formula are consistent with the $RMSE$ of the bulk-aerodynamic formula based results (Table 5 and Fig. 3). B1 performs better than B2 and B3, with the lowest σ_{H_s} and σ_{H_i} . For the sensible heat flux, T_s contributes the most to the estimated error, followed by T_r . For the latent heat flux, Q_s or Q_r is the major contributor to the estimated error for the three results. C_H and C_E show limited contributions (3%–13%) to the estimated error, compared with the surface/air temperature and specific humidity. The contributions from ρ_a , c_p , and L_v are negligible ($\leq 5\%$).

The estimated errors for the MEP-based results are 25%–70% lower than the real $RMSE$ of the MEP-based results

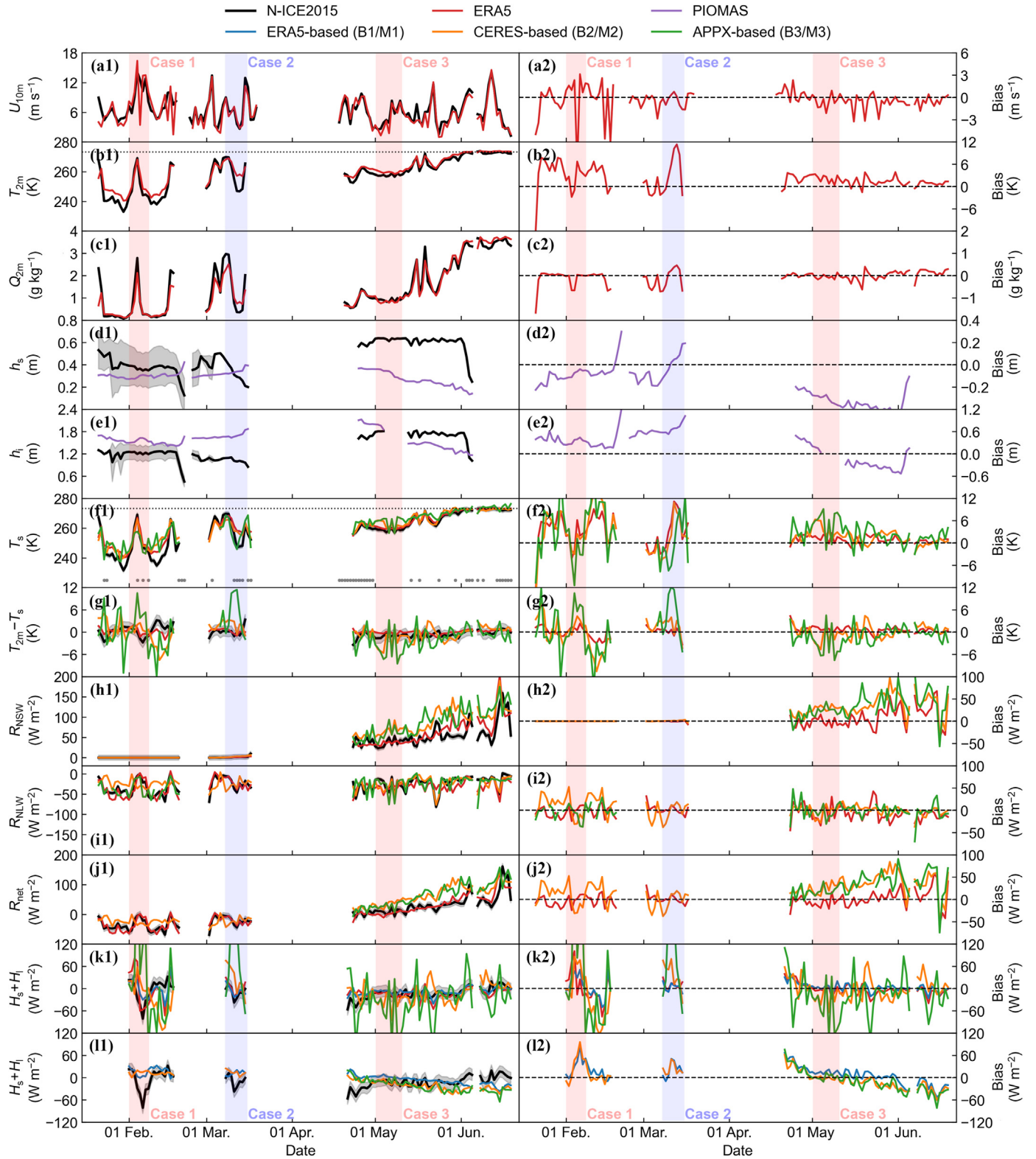


Fig. 4. Comparison of surface and near surface parameters from satellite estimates, ERA5 reanalysis and N-ICE2015 observations, (a) 10-m wind speed, (b) 2-m air temperature, (c) 2-m specific humidity, (d) snow depth over sea ice, (e) sea ice thickness, (f) ice surface temperature, (g) 2-m air temperature minus ice surface temperature, (h) net shortwave radiative flux, (i) net longwave radiative flux, (j) net radiative flux, (k) bulk-formula based turbulent heat flux, and (l) MEP-based turbulent heat flux ((a1–l1) show the time series of the parameters and (a2–l2) represent their biases to the *in-situ* observations. Uncertainties in the N-ICE2015 gridded observations are shaded in grey in (a1–l1). The temperature of 0 °C is shown in dotted line in (b1) and (f1). Days with sea ice concentration less than 95% are shown in grey dots in (f1)).

Table 6
Correlation coefficients (r) between the turbulent heat fluxes (sum of the sensible heat flux and latent heat flux) and surface/near surface parameters from *in-situ* observations, ERA5 reanalysis and satellite estimates.

Parameter	N-ICE2015	ERA5	B1	B2	B3	M1	M2	M3
U_{10m}	-0.09	0.11	0	0.09	0.18	0.07	0.30	-0.06
T_{2m}	0.14	0.11	0.18	0.27	0.09	-0.89	-0.71	-0.83
Q_{2m}	0.31	0.15	0.26	0.30	0.09	-0.86	-0.67	-0.78
h_s	-0.20	0.03	-0.10	0.01	0.03	0.60	0.63	0.74
h_i	-0.20	0.01	-0.14	0.09	0.01	0.32	0.39	0.79
T_s	0.04	0.04	0.10	0.04	-0.32	-0.89	-0.75	-0.81
$T_{2m} - T_s$	0.73	0.83	0.87	0.91	0.89	-0.11	0.03	-0.28
R_{NSW}	0.11	-0.07	0.04	0	0.40	-0.87	-0.92	-0.78
R_{NLW}	-0.03	-0.02	0.09	-0.10	-0.01	-0.46	-0.36	-0.53
R_{net}	0.08	-0.07	0.07	-0.03	0.29	-0.98	-0.98	-0.93

Note: B1–B3 and M1–M3 represent turbulent heat flux estimates using bulk-formula and MEP method, respectively. The snow depth and sea ice thickness are from PIOMAS for ERA5, B1–B3, and M1–M3. The 10-m wind speed, 2-m air temperature and 2-m specific humidity are from ERA5 for B1–B3, and M1–M3. The bold text represents the largest absolute value for each parameter.

Table 7
Biases of the input parameters in the bulk-aerodynamic formula and MEP and their contributions to the overall uncertainties.

Type	Group	Biases of inputs (Contribution to the overall uncertainty, %)									σ_{H_s} ($W m^{-2}$)
		ρ_a ($kg m^{-3}$)	c_p ($J kg^{-1} K^{-1}$)	C_H ($\times 10^3$)	U_{10m} ($m s^{-1}$)	T_{2m} (K)	T_s (K)	R_{net} ($W m^{-2}$)	h_s (m)	h_i (m)	
Sensible heat flux	B1	0.13 (1)	1.0 (0)	-0.09 (3)	-0.35 (4)	<u>2.1 (44)</u>	1.8 (48)	–	–	–	39.3
	B2	0.13 (3)	1.0 (0)	-0.03 (7)	-0.35 (9)	<u>2.1 (36)</u>	2.4 (45)	–	–	–	46.2
	B3	0.13 (4)	1.0 (0)	-0.03 (10)	-0.35 (11)	<u>2.1 (27)</u>	2.7 (49)	–	–	–	66.3
	M1	0.13 (4)	1.0 (0)	–	–	–	1.8 (2)	9.4 (66)	<u>-0.22 (20)</u>	0.10 (5)	6.2
	M2	0.13 (2)	1.0 (0)	–	–	–	2.4 (2)	20.6 (65)	<u>-0.22 (23)</u>	0.10 (4)	11.2
	M3	0.13 (3)	1.0 (0)	–	–	–	2.7 (2)	33.3 (60)	<u>-0.22 (27)</u>	0.10 (4)	12.6
Type	Case	ρ_a ($kg m^{-3}$)	L_v ($\times 10^6 J kg^{-2}$)	C_E ($\times 10^3$)	U_{10m} ($m s^{-1}$)	Q_{2m} ($g kg^{-1}$)	Q_s ($g kg^{-1}$)	R_{net} ($W m^{-2}$)	h_s (m)	h_i (m)	σ_{H_i} ($W m^{-2}$)
Latent heat flux	B1	0.13 (3)	0.43 (5)	-0.09 (5)	-0.35 (10)	-0.02 (42)	<u>0.14 (35)</u>	–	–	–	11.3
	B2	0.13 (4)	0.43 (6)	-0.03 (7)	-0.35 (9)	<u>-0.02 (35)</u>	0.20 (38)	–	–	–	13.3
	B3	0.13 (5)	0.43 (7)	-0.03 (7)	-0.35 (9)	<u>-0.02 (23)</u>	0.33 (49)	–	–	–	21.8
	M1	0.13 (2)	0.43 (11)	–	–	–	0.14 (9)	9.4 (51)	<u>-0.22 (21)</u>	0.10 (4)	2.9
	M2	0.13 (2)	0.43 (12)	–	–	–	0.20 (8)	20.6 (49)	<u>-0.22 (25)</u>	0.10 (4)	5.4
	M3	0.13 (2)	0.43 (12)	–	–	–	0.33 (8)	33.3 (49)	<u>-0.22 (27)</u>	0.10 (4)	7.7

Note: B1–B3 and M1–M3 represent turbulent heat flux estimates using bulk-formula and MEP method, respectively. The bold (underlined) text represents the parameter with largest (second largest) contribution to the overall uncertainties.

(Table 5). It should be noted that the error propagation function can only represent the total uncertainty contributed by each variable in the parameterization scheme, rather than the real performance of the parameterization. Thus, the larger *RMSE* (calculated against the *in-situ* observations) of the MEP estimates with a smaller estimated error (calculated by the error propagation functions) indicates the deficiency of the MEP scheme in capturing turbulent fluxes in N-ICE2015 ice conditions. This may result from: 1) insufficient representation of the wind effect on the thermal inertia I_s (see Section 3.1.2); and 2) cases of sea ice and open water mixing (Fig. 2). Nevertheless, the relative performance of the three estimates remains unchanged, in that M1 still outperforms M2 and M3, with lower σ_{H_s} and σ_{H_i} . For the sensible heat flux, the uncertainties of the net radiative fluxes dominate the total error (>50%). T_s has a fairly small impact on the estimated error ($\leq 3\%$). Although, physically, the effect of the radiative fluxes on the turbulent fluxes comes via the effect of the radiative fluxes on the ice surface temperature, the percentage error of the radiative fluxes (13%–49%) for the gridded products is at

least an order of magnitude larger than that of the ice surface temperature ($\sim 1\%$), resulting in a stronger contribution of radiative fluxes to the estimated uncertainties. In addition, h_s makes a moderate contribution to the error (20%–30%) by controlling the absorption of the net shortwave radiation over the ice surface (see Section 3.1.2). For the latent heat flux, the radiative fluxes and h_s are still the primary and secondary contributors to the error, while the contribution of T_s is close to 10%.

5. Discussion

5.1. Potential causes of errors in the turbulent heat flux estimates

As shown in Section 4.2 and 4.3, the observed turbulent heat fluxes based on the bulk-aerodynamic formula strongly rely on the air–ice temperature gradient, thus the errors in the surface and air temperature from reanalysis and satellite products could explain most of the uncertainties of the

turbulent heat flux estimates. For the ERA5 reanalysis, a slight warm bias of 2-m air temperature (~ 2 K) could be seen throughout the N-ICE2015 period (Table 7). Larger overestimation (>10 K) usually occurs during the cold periods when temperature decreases below -25 °C (Fig. 4), which may be due to deficiencies in characterizing strong vertical temperature gradients in strongly stable boundary layer (Cuxart et al., 2006; Serreze et al., 2012). Similar warm biases exist in the ice surface temperature in ERA5, CERES, and APP-X, and are likely attributed to the missing representation of the insulating effect of snow on the ice surface (Batak and Müller, 2019; Vihma et al., 2002). Additionally, the surface radiation budget plays the most important role in the MEP-based estimates. Positive biases in the surface radiative fluxes mainly come from the overestimation of shortwave component for either ERA5, CERES or APP-X. The biases increase in the melt season (late spring to summer), when these products show difficulties in resolving cloud, surface temperature, and albedo (di Biagio et al., 2021; Wang et al., 2019). It should be noted that the wind speed, temperature, and humidity profiles from various satellite and *in-situ* observations have been assimilated in ERA5, which may improve its performance (Hersbach et al., 2020). Besides, significant fluctuations have been observed in surface temperature, radiative fluxes and derived turbulent heat fluxes for APP-X. It may partly be due to the coarser temporal resolution (twice daily) compared to ERA5 and CERES (hourly).

In addition, the different parameterization schemes impact the turbulent heat flux estimates. By using the surface and near surface parameters from N-ICE2015 point observations as inputs in bulk-formula and MEP, we compared the estimated turbulent heat fluxes with the point measurements (over sea ice) (Figs. A1 and A2). The bulk-formula based estimates agree better with the *in-situ* measurements for the sensible heat flux ($r > 0.6$ and $MB < 5 \text{ W m}^{-2}$) than the latent heat flux. It indicates that the SHEBA parameterization, which is based on observations over thicker multi-year ice in the Beaufort Sea 25 years ago, is still applicable to the N-ICE2015 sea ice conditions but may need further improvements in the context of the changing Arctic. MEP even outperforms the bulk-formula with smaller bias and *RMSEs*, particularly when applied over a homogeneous ice surface (100% sea ice concentration) rather than the heterogeneous ones (with a fraction of open water). Thus, further improvements should focus on the energy budget in the marginal ice zone, e.g., the radiative transfer processes and the moisture exchanges.

5.2. Gridded products vs. point observations

Additional biases would be expected when comparing *in-situ* point measurement with the average values of grid cells from satellite observations or reanalysis due to the scale difference, especially for heterogeneous surface. We mitigated these biases by adjusting the N-ICE2015 point observations to equivalent ‘gridded’ ones. We noticed that the shortwave radiative fluxes and the turbulent heat fluxes increase

significantly when the open water fraction was considered. By providing reasonable uncertainties, we recommend this kind of adjustment to *in-situ* point measurements over sea ice for better match with gridded products. In turn, the satellite and reanalysis products should further separate the contribution from sea ice and open water to the surface energy budget components in the grid cells.

5.3. Improvements and limitations

Given that numerous Arctic climate change studies rely heavily on satellite- and reanalysis-based surface energy components, or numerical simulations forced by these data, the choice of these products should be considered with prudence (Beer et al., 2020; Lindsay et al., 2014; Vihma, 2014). For the first time, the dependability of current satellite- and reanalyses-based turbulent heat fluxes over Arctic sea ice was revealed. We recommended ERA5 as the first choice, followed by CERES and APP-X, though with considerable uncertainties ($>200\%$). This study, together with di Biagio et al. (2021) and Graham et al. (2019), draws a picture of the reliability of the satellite observations and atmospheric reanalyses in the context of the surface energy budget over Arctic sea ice. We also demonstrated the applicability of the traditional bulk-formula and the MEP method in deriving turbulent heat fluxes from satellite observations, which will benefit the satellite retrieval of pan-Arctic surface turbulent heat fluxes during the last two decades in further study.

Nevertheless, there are still limitations in this study. The comparison and evaluation only cover the winter to early summer in one year, and limited on single site over young ice in the Atlantic sector of the Arctic. This is due to the lack of simultaneous *in-situ* observations of atmosphere, ocean, and sea ice in the Arctic. With the release of data from the year-round *in-situ* measurements over Arctic sea ice, i.e., Multi-disciplinary drifting Observatory for the Study of Arctic Climate (MOSAiC, 2019–2020), more comprehensive evaluations of the surface energy budget from satellite observations, reanalyses and model simulations are expected, to identify the regions and seasons where these gridded products provide reliable estimates. In addition, application of new turbulent flux parameterizations (e.g., Elvidge et al., 2021; Lüpkes and Gryanik, 2015) and their inter-comparisons are welcomed, to recognize their reliabilities in delineating the turbulent flux of momentum and heat over Arctic sea ice, especially in the regions sensitive to the climate change, e.g., leads, polynyas, and marginal ice zones.

6. Conclusions

The bulk-formula based estimates could generally capture the variation and trends of the measured turbulent heat fluxes, compared to the entropy-based ones, and perform better in summer (winter) for the sensible (latent) heat flux. CERES-based estimates outperform the APP-X-based results, whereas ERA5 performs the best in all seasons (*RMSE* of 18 and 7 W m^{-2} for the sensible and latent heat flux,

respectively). Nevertheless, the satellite-based estimates with entropy method show comparable *RMSEs* to the ERA5 reanalysis. Case studies and overall analysis confirmed that the bulk-formula strongly relies on the air–ice gradient while the entropy method is primarily driven by the surface radiation budget. Thus, among the input variables in the turbulent heat flux models, the errors in the surface and near surface temperature/humidity contribute most (close to 50%) to the uncertainties in the estimates based on the bulk-formula, and so as the net radiative fluxes (>50%) to the entropy-based results.

Declaration of competing interest

The authors declare no conflict of interest.

Acknowledgments

This work was supported by the National Natural Science Foundation of China (41976214). The European Union's Horizon 2020 research and innovation programme provided support to BC and TV through the Polar Regions in the Earth System project (PolarRES, 101003590), and to MAG through the Climate Relevant interactions and feedbacks: the key role of sea ice and Snow in the polar and global climate system project (CRiceS, 101003826).

The authors would like to thank the National Aeronautics and Space Administration (NASA) for providing the CERES data, the National Oceanic and Atmospheric Administration (NOAA) for providing the APP-X data, the University of Bremen for providing the AMSR2 sea ice concentration data, the European Centre for Medium-Range Weather Forecasts (ECMWF) for providing the ERA5 data, the University of Washington for providing the PIOMAS data, and the Norwegian Polar Institute (NPI) for providing the N-ICE2015 observation datasets. The N-ICE2015 field observations were carried by an international team and supported by the NPI, the Ministry of Climate and Environment, and the Ministry of Foreign Affairs of Norway.

Appendix A. Supplementary data

Supplementary data to this article can be found online at <https://doi.org/10.1016/j.accre.2023.04.004>.

References

Adams, S., Willmes, S., Schröder, D., et al., 2012. Improvement and sensitivity analysis of thermal thin-ice thickness retrievals. *IEEE Trans. Geosci. Rem. Sens.* 51, 3306–3318.

Andreas, E.L., 1987. A theory for the scalar roughness and the scalar transfer coefficients over snow and sea ice. *Boundary-Layer Meteorol.* 38, 159–184.

Andreas, E.L., Horst, T.W., Grachev, A.A., et al., 2010a. Parametrizing turbulent exchange over summer sea ice and the marginal ice zone. *Q. J. R. Meteorol. Soc.* 136, 927–943.

Andreas, E.L., Persson, P.O.G., Grachev, A.A., et al., 2010b. Parameterizing turbulent exchange over sea ice in winter. *J. Hydrometeorol.* 11, 87–104.

Arndt, S., Nicolaus, M., 2014. Seasonal cycle and long-term trend of solar energy fluxes through Arctic sea ice. *Cryosphere* 8, 2219–2233.

Batrak, Y., Müller, M., 2019. On the warm bias in atmospheric reanalyses induced by the missing snow over Arctic sea–ice. *Nat. Commun.* 10, 1–8.

Beer, E., Eisenman, I., Wagner, T.J., 2020. Polar amplification due to enhanced heat flux across the halocline. *Geophys. Res. Lett.* 47, e2019GL086706.

Blanchard, Y., Pelon, J., Eloranta, E.W., et al., 2014. A synergistic analysis of cloud cover and vertical distribution from A-Train and ground-based sensors over the high Arctic station EUREKA from 2006 to 2010. *J. Appl. Meteorol. Climatol.* 53, 2553–2570.

Boisvert, L., Wu, D., Shie, C.L., 2015a. Increasing evaporation amounts seen in the Arctic between 2003 and 2013 from AIRS data. *J. Geophys. Res. Atmos.* 120, 6865–6881.

Boisvert, L., Wu, D., Vihma, T., et al., 2015b. Verification of air/surface humidity differences from AIRS and ERA-Interim in support of turbulent flux estimation in the Arctic. *J. Geophys. Res. Atmos.* 120, 945–963.

Boisvert, L.N., Markus, T., Vihma, T., 2013. Moisture flux changes and trends for the entire Arctic in 2003–2011 derived from EOS Aqua data. *J. Geophys. Res. Oceans* 118, 5829–5843.

Cohen, J., Screen, J.A., Furtado, J.C., et al., 2014. Recent Arctic amplification and extreme mid-latitude weather. *Nat. Geosci.* 7, 627–637.

Cohen, L., Hudson, S.R., Walden, V.P., et al., 2017. Meteorological conditions in a thinner Arctic sea ice regime from winter to summer during the Norwegian Young Sea Ice expedition (N-ICE2015). *J. Geophys. Res. Atmos.* 122, 7235–7259.

Cuxart, J., Holtstlag, A.A., Beare, R.J., et al., 2006. Single-column model intercomparison for a stably stratified atmospheric boundary layer. *Boundary-Layer Meteorol.* 118, 273–303.

Dai, A., Luo, D., Song, M., et al., 2019. Arctic amplification is caused by sea–ice loss under increasing CO₂. *Nat. Commun.* 10, 1–13.

di Biagio, C., Pelon, J., Blanchard, Y., et al., 2021. Toward a better surface radiation budget analysis over sea ice in the high Arctic Ocean: a comparative study between satellite, reanalysis, and local-scale observations. *J. Geophys. Res. Atmos.* 126, e2020JD032555.

Doelling, D.R., Sun, M., Nguyen, L.T., et al., 2016. Advances in geostationary-derived longwave fluxes for the CERES synoptic (SYN1deg) product. *J. Atmos. Ocean. Technol.* 33, 503–521.

ECMWF, 2021. IFS Documentation – Cy47r3. Part IV: Physical Processes, pp. 37–40.

Elvidge, A.D., Renfrew, I.A., Brooks, I.M., et al., 2021. Surface heat and moisture exchange in the marginal ice zone: observations and a new parameterization scheme for weather and climate models. *J. Geophys. Res. Atmos.* 126, e2021JD034827.

Fairall, C.W., Bradley, E.F., Rogers, D.P., et al., 1996. Bulk parameterization of air–sea fluxes for tropical ocean–global atmosphere coupled–ocean atmosphere response experiment. *J. Geophys. Res. Oceans* 101, 3747–3764.

Feldl, N., Merlis, T.M., 2021. Polar amplification in idealized climates: the role of ice, moisture, and seasons. *Geophys. Res. Lett.* 48, e2021GL094130.

Feldman, D.R., Collins, W.D., Pincus, R., et al., 2014. Far-infrared surface emissivity and climate. *Proc. Natl. Acad. Sci. USA* 111, 16297–16302.

Grachev, A.A., Andreas, E.L., Fairall, C.W., et al., 2007. SHEBA flux–profile relationships in the stable atmospheric boundary layer. *Boundary-Layer Meteorol.* 124, 315–333.

Graham, R.M., Cohen, L., Ritzhaupt, N., et al., 2019. Evaluation of six atmospheric reanalyses over Arctic sea ice from winter to early summer. *J. Clim.* 32, 4121–4143.

Granskog, M.A., Assmy, P., Gerland, S., et al., 2016. Arctic research on thin ice: consequences of Arctic sea ice loss. *Eos Trans. AGU* 97, 22–26.

Granskog, M.A., Fer, I., Rinke, A., et al., 2018. Atmosphere–ice–ocean–ecosystem processes in a thinner Arctic sea ice regime: the Norwegian Young Sea ICE (N-ICE2015) expedition. *J. Geophys. Res. Oceans* 123, 1586–1594.

Hersbach, H., Bell, B., Berrisford, P., et al., 2018. ERA5 hourly data on single levels from 1979 to present. In: Copernicus Climate Change Service (C3S) Climate Data Store (CDS). <https://doi.org/10.24381/cds.adbb2d47>.

Hersbach, H., Bell, B., Berrisford, P., et al., 2020. The ERA5 global reanalysis. *Q. J. R. Meteorol. Soc.* 146, 1999–2049.

- Hudson, S.R., Cohen, L., Walden, V.P., 2015. N-ICE2015 surface meteorology [data set]. Norwegian Polar Institute. <https://doi.org/10.21334/npolar.2015.056a61d1>.
- Hudson, S.R., Cohen, L., Walden, V.P., 2016. N-ICE2015 surface broadband radiation data [data set]. Norwegian Polar Institute. <https://doi.org/10.21334/npolar.2016.a89cb766>.
- IPCC, 2019. Special Report on the Ocean and Cryosphere in a Changing Climate. Cambridge University Press, Cambridge and New York.
- IPCC, 2021. Climate Change 2021: The Physical Science Basis. Contribution of Working Group I to the Sixth Assessment Report of the Intergovernmental Panel on Climate Change. Cambridge University Press, Cambridge and New York.
- Itkin, P., Spreen, G., Cheng, B., et al., 2015. N-ICE2015 buoy data [data set]. Norwegian Polar Institute. <https://doi.org/10.21334/npolar.2015.6ed9a8ca>.
- Jakobson, E., Vihma, T., Palo, T., et al., 2012. Validation of atmospheric reanalyses over the central Arctic Ocean. *Geophys. Res. Lett.* 39, L10802. <https://doi.org/10.1029/2012GL051591>.
- Jonassen, M.O., Välisuo, I., Vihma, T., et al., 2019. Assessment of atmospheric reanalyses with independent observations in the Weddell Sea, the Antarctic. *J. Geophys. Res. Atmos.* 124, 12468–12484.
- Jordan, R.E., Andreas, E.L., Makshtas, A.P., 1999. Heat budget of snow-covered sea ice at North Pole 4. *J. Geophys. Res. Oceans* 104, 7785–7806.
- Kacimi, S., Kwok, R., 2022. Arctic snow depth, ice thickness and volume from ICESat-2 and CryoSat-2: 2018–2021. *Geophys. Res. Lett.*, e2021GL097448
- Key, J., 2016. NOAA climate data record (CDR) of AVHRR polar pathfinder extended (APP-X) cryosphere. NOAA. <https://doi.org/10.25921/AE96-0E57>.
- Key, J., Wang, X., Liu, Y., et al., 2016. The AVHRR polar pathfinder climate data records. *Rem. Sens.* 8, 167.
- Key, J.R., Schweiger, A.J., 1998. Tools for atmospheric radiative transfer: streamer and fluxNet. *Comput. Geosci.* 24, 443–451.
- Kwok, R., 2018. Arctic sea ice thickness, volume, and multiyear ice coverage: losses and coupled variability (1958–2018). *Environ. Res. Lett.* 13, 105005.
- Lenaerts, J.T., Van Tricht, K., Lhermitte, S., et al., 2017. Polar clouds and radiation in satellite observations, reanalyses, and climate models. *Geophys. Res. Lett.* 44, 3355–3364.
- Lindsay, R., Wensnahan, M., Schweiger, A., et al., 2014. Evaluation of seven different atmospheric reanalysis products in the Arctic. *J. Clim.* 27, 2588–2606.
- Loeb, N.G., Doelling, D.R., Wang, H., et al., 2018. Clouds and the Earth's radiant energy system (CERES) energy balanced and filled (EBAF) top-of-atmosphere (TOA) edition-4.0 data product. *J. Clim.* 31, 895–918.
- Lüpkes, C., Gryanik, V.M., 2015. A stability-dependent parametrization of transfer coefficients for momentum and heat over polar sea ice to be used in climate models. *J. Geophys. Res. Atmos.* 120, 552–581.
- Lüpkes, C., Gryanik, V.M., Hartmann, J., et al., 2012. A parametrization, based on sea ice morphology, of the neutral atmospheric drag coefficients for weather prediction and climate models. *J. Geophys. Res.* 117.
- Lüpkes, C., Vihma, T., Jakobson, E., et al., 2010. Meteorological observations from ship cruises during summer to the central Arctic: a comparison with reanalysis data. *Geophys. Res. Lett.* 37.
- Maykut, G.A., 1982. Large-scale heat exchange and ice production in the central Arctic. *J. Geophys. Res. Oceans* 87, 7971–7984.
- Merkouriadis, I., Liston, G.E., Graham, R.M., et al., 2020. Quantifying the potential for snow–ice formation in the Arctic Ocean. *Geophys. Res. Lett.* 47.
- Monin, A., Obukhov, A., 2002. Dimensionless characteristics of turbulence in the surface layer, 1954 Akad. Nank. SSSR. *Geofiz. Inst.* 12–26.
- Paulson, C.A., 1970. The mathematical representation of wind speed and temperature profiles in the unstable atmospheric surface layer. *J. Appl. Meteorol. Climatol.* 9, 857–861.
- Pond, S., Fissel, D., Paulson, C., 1974. A note on bulk aerodynamic coefficients for sensible heat and moisture fluxes. *Boundary-Layer Meteorol.* 6, 333–339.
- Preußner, A., Heinemann, G., Willmes, S., et al., 2016. Circumpolar polynya regions and ice production in the Arctic: results from MODIS thermal infrared imagery from 2002/2003 to 2014/2015 with a regional focus on the Laptev Sea. *Cryosphere* 10, 3021–3042.
- Qu, M., Pang, X., Zhao, X., et al., 2021. Spring leads in the Beaufort Sea and its interannual trend using Terra/MODIS thermal imagery. *Rem. Sens. Environ.* 256, 112342.
- Qu, M., Pang, X., Zhao, X., et al., 2019. Estimation of turbulent heat flux over leads using satellite thermal images. *Cryosphere* 13, 1565–1582.
- Ray, M., Rogers, A., McGowan, J., 2006. Analysis of wind shear models and trends in different terrains. University of Massachusetts.
- Renfrew, I.A., Barrell, C., Elvidge, A., et al., 2021. An evaluation of surface meteorology and fluxes over the Iceland and Greenland Seas in ERA5 reanalysis: the impact of sea ice distribution. *Q. J. R. Meteorol. Soc.* 147, 691–712.
- Riihela, A., Bright, R.M., Anttila, K., 2021. Recent strengthening of snow and ice albedo feedback driven by Antarctic sea–ice loss. *Nat. Geosci.* 14, 832–836.
- Rösel, A., Itkin, P., King, J., et al., 2018. Thin sea ice, thick snow, and widespread negative freeboard observed during N-ICE2015 north of Svalbard. *J. Geophys. Res. Oceans* 123, 1156–1176.
- Schröder, D., Feltham, D.L., Flocco, D., et al., 2014. Arctic sea–ice minimum predicted by spring melt-pond fraction. *Nat. Clim. Change* 4, 353–357.
- Schweiger, A., Lindsay, R., Zhang, J., et al., 2011. Uncertainty in modeled Arctic sea ice volume. *J. Geophys. Res. Oceans* 116.
- Serreze, M.C., Barrett, A.P., Slater, A.G., et al., 2007. The large-scale energy budget of the Arctic. *J. Geophys. Res. Atmos.* 112.
- Serreze, M.C., Barrett, A.P., Stroeve, J., 2012. Recent changes in tropospheric water vapor over the Arctic as assessed from radiosondes and atmospheric reanalyses. *J. Geophys. Res. Atmos.* 117.
- Spreen, G., Kaleschke, L., Heygster, G., 2008. Sea ice remote sensing using AMSR-E89-GHz channels. *J. Geophys. Res. Oceans* 113.
- Stroeve, J., Barrett, A., Serreze, M., et al., 2014. Using records from submarine, aircraft and satellites to evaluate climate model simulations of Arctic sea ice thickness. *Cryosphere* 8, 1839–1854.
- Tamura, T., Ohshima, K.I., 2011. Mapping of sea ice production in the Arctic coastal polynyas. *J. Geophys. Res. Oceans* 116.
- van Tricht, K., Lhermitte, S., Gorodetskaya, I.V., et al., 2016. Improving satellite-retrieved surface radiative fluxes in polar regions using a smart sampling approach. *Cryosphere* 10, 2379–2397.
- Vihma, T., 1995. Subgrid parameterization of surface heat and momentum fluxes over polar oceans. *J. Geophys. Res. Oceans* 100, 22625–22646.
- Vihma, T., 2014. Effects of Arctic sea ice decline on weather and climate: a review. *Surv. Geophys.* 35, 1175–1214.
- Vihma, T., Uotila, J., Cheng, B., et al., 2002. Surface heat budget over the Weddell Sea: buoy results and model comparisons. *J. Geophys. Res. Oceans* 107, 5-1-5-15.
- Vihma, T., Uotila, J., Launiainen, J., 1998. Air–sea interaction over a thermal marine front in the Denmark Strait. *J. Geophys. Res. Oceans* 103, 27665–27678.
- Walden, V.P., Hudson, S.R., Cohen, L., et al., 2017a. Atmospheric components of the surface energy budget over young sea ice: results from the N-ICE2015 campaign. *J. Geophys. Res. Atmos.* 122, 8427–8446.
- Walden, V.P., Murphy, S., Hudson, S.R., et al., 2017b. N-ICE2015 atmospheric turbulent fluxes [data set]. Norwegian Polar Institute. <https://doi.org/10.21334/npolar.2017.298013b7>.
- Wang, C., Graham, R.M., Wang, K., et al., 2019. Comparison of ERA5 and ERA-Interim near-surface air temperature, snowfall and precipitation over Arctic sea ice: effects on sea ice thermodynamics and evolution. *Cryosphere* 13, 1661–1679.
- Wang, G., Wang, T., Xue, H., 2021. Validation and comparison of surface shortwave and longwave radiation products over the three poles. *Int. J. Appl. Earth Obs. Geoinf.* 104, 102538.
- Wang, J., Bras, R., 2011. A model of evapotranspiration based on the theory of maximum entropy production. *Water Resour. Res.* 47.
- Wang, J., Bras, R.L., 2009. A model of surface heat fluxes based on the theory of maximum entropy production. *Water Resour. Res.* 45.
- Wang, J., Bras, R.L., Nieves, V., et al., 2014. A model of energy budgets over water, snow, and ice surfaces. *J. Geophys. Res. Atmos.* 119, 6034–6051.

- You, C., Tjernström, M., Devasthale, A., 2021. Eulerian and Lagrangian views of warm and moist air intrusions into summer Arctic. *Atmospheric Res.* 256, 105586.
- Zhang, J., Rothrock, D.A., 2003. Modeling global sea ice with a thickness and enthalpy distribution model in generalized curvilinear coordinates. *Mon. Weather Rev.* 131, 845–861.
- Zhang, X., Fu, Y., Han, Z., et al., 2021a. Extreme cold events from East Asia to North America in winter 2020/21: comparisons, causes, and future implications. *Adv. Atmos. Sci.* 39 (4), 553–565.
- Zhang, Y.-M., Song, M.-R., Dong, C.-M., et al., 2021b. Modeling turbulent heat fluxes over Arctic sea ice using a maximum-entropy-production approach. *Adv. Clim. Change Res.* 12, 517–526.